Society of Medical Education & Research

2021, Volume 1, Page No: 66-84
ISSN: 3108-4834

Archive of International Journal of Cancer and Allied Science

Inhibition of Estrogen-Related Receptor-α Suppresses Mitochondrial Oxidative Phosphorylation and Decreases M2 Macrophage Infiltration in Endometrial Cancer

Kenji Hiroto Sakamoto[1]*, Naoki Jun Takahashi[1]

[1]Division of Cancer Biology, Keio University School of Medicine, Tokyo, Japan.

***E-mail** ✉ k.sakamoto.keio@outlook.com

Abstract

Endometrial cancer (EC) is a gynecologic malignancy closely associated with disruptions in metabolic processes. A majority of EC patients respond poorly to immunotherapy, highlighting the urgent need to identify novel therapeutic targets at the interface of metabolism and immune regulation. In vitro, a combination of proteomics, CUT&Tag (cleavage under targets and tagmentation) sequencing, dual-luciferase reporter assays, lipidomic profiling, and macrophage–tumor co-culture systems was employed to reveal the dual metabolic and immunomodulatory role of estrogen-related receptor α (ERRα) in KLE and HEC-1A human EC cell lines. Patient-derived organoids were utilized to confirm the therapeutic potential of ERRα inhibition. In vivo, KLE xenografts were used to examine tumor progression and assess treatment efficacy in mice. Clinically, a retrospective cohort of 166 EC patients was analyzed via immunohistochemistry (IHC) to evaluate ERRα expression and macrophage infiltration, allowing correlation with disease features and therapeutic relevance. Multiplex IHC was applied to examine the spatial distribution of M2 macrophages during EC progression.

ERRα directly binds to the PTPMT1 promoter region (-624 to −609 bp), driving its transcription in EC cells. This upregulation enhances cardiolipin biosynthesis, which stabilizes the inner mitochondrial membrane, boosts oxidative phosphorylation (OXPHOS), and increases reactive oxygen species (ROS) levels. Elevated ROS subsequently activates NF-κB signaling, promoting CCL2 secretion and recruiting M2 macrophages into the tumor microenvironment. Combined inhibition of ERRα (XCT790) and CCL2 (carlumab) produced significantly enhanced antitumor effects in EC. Moreover, ERRα expression in patient tissues may serve as a biomarker for disease assessment. These findings uncover a critical role for the ERRα-driven metabolic axis in shaping the immune landscape of EC, linking mitochondrial lipid metabolism to macrophage-mediated immunosuppression. This work provides mechanistic insight supporting combined metabolic–immune-targeted therapies as a strategy to overcome immunotherapy resistance in EC.

Keywords: Mitochondria, Macrophage, Cytokine, Endometrial cancer

Introduction

Over the past 30 years, the incidence of endometrial cancer (EC) has risen by 132%, with diagnoses increasingly occurring in younger women [1]. Early-stage EC (FIGO stages I–II) has a 5-year survival rate of 74–91%, whereas patients with stage III disease show survival rates of 57–66%, and stage IV disease is associated with only 20–26% 5-year survival [2]. Previous work indicates that estrogen-related receptor α (ERRα/ESRRA) is overexpressed in EC [3] and drives lipid reprogramming, contributing to tumor invasion and metastasis [4]. ERRα also transcriptionally regulates mitochondrial metabolic pathways, including OXPHOS, the tricarboxylic acid cycle, and fatty acid β-oxidation [5].

Cardiolipins (CLs), essential lipids of the inner mitochondrial membrane, play a critical role in mitochondrial metabolism, including electron transport and OXPHOS [6]. Protein tyrosine phosphatase mitochondrial 1 (PTPMT1) is a mitochondrial tyrosine

Access this article online https://smerpub.com/

Received: 19 October 2020; **Accepted:** 26 January 2021

How to cite this article: Sakamoto KH, Takahashi NJ. Inhibition of Estrogen-Related Receptor-α Suppresses Mitochondrial Oxidative Phosphorylation and Decreases M2 Macrophage Infiltration in Endometrial Cancer. Arch Int J Cancer Allied Sci. 2021;1:66-84. https://doi.org/10.51847/UuEU7UzmyS

phosphatase that regulates mitochondrial morphology and metabolism through CL biosynthesis [7]. Aberrant PTPMT1 expression has been observed across multiple cancer types, including breast [8], lung [9], hepatocellular [10], and pancreatic cancers [11], often correlating with advanced stage, aggressive tumor behavior, and poor prognosis [8, 10]. ERRα has been shown to enhance CL synthesis in breast cancer cells [12], while CL-induced mitochondrial autophagy can suppress tumorigenesis in pancreatic, lung, and colon cancers [13]. However, the regulatory relationship between ERRα and PTPMT1 in EC, and its impact on mitochondrial function, remains unexplored.

Recent studies have highlighted ERRα's involvement in both tumor metabolism and immune regulation [14]. ERRα inhibition impairs tumor energy metabolism and stimulates immune responses by inducing proinflammatory cytokine production, promoting macrophage polarization, and enhancing CD8+ T-cell recruitment [14]. EC is considered a "cold tumor," characterized by low T-cell infiltration; single-cell transcriptome analysis revealed reduced cytotoxic CD8+ T cells in endometrioid adenocarcinoma compared to normal tissue [15]. Conversely, macrophages are enriched in all pathological EC subtypes, including endometrioid adenocarcinoma, uterine serous carcinoma, and clear cell carcinoma [16]. Immunotherapy targeting PD-1 has limited efficacy in advanced EC or in microsatellite instability-high tumors, though combination with chemotherapy improves outcomes [17].

Macrophages and lymphocytes constitute a large portion of the EC immune landscape, with M2 macrophages predominating [15, 18]. These cells facilitate tumor angiogenesis, epithelial–mesenchymal transition (EMT), immune evasion, and metastasis via cytokine secretion and interactions with other immune cells [19, 20]. ERRα has been implicated in macrophage modulation, affecting polarization and cytokine output [21]; however, its role in regulating M2 macrophages within EC remains underexplored. This study investigates how ERRα in EC cells promotes M2 macrophage recruitment through mitochondrial OXPHOS regulation, aiming to elucidate mechanisms that may inform novel therapeutic strategies for improving patient outcomes.

Materials and Methods

Cell lines and culture

Human endometrial cancer cell lines KLE (ATCC, Maryland, USA), HEC-1A (National Collection of Authenticated Cell Cultures, Shanghai, China), and the monocyte cell line THP-1 (National Collection of Authenticated Cell Cultures, Shanghai, China) were maintained in DMEM/F12 or McCoy's 5A media, each supplemented with 10 percent fetal bovine serum (FBS; #10091148, Gibco, New Zealand) and 1 percent penicillin-streptomycin (#15140122, Gibco) at 37°C in a humidified atmosphere containing 5% CO_2. Authentication of all cell lines was confirmed through short tandem repeat (STR) profiling. Lentiviral vectors were utilized to modulate gene expression: ERRα knockdown was achieved using LV-sh-ESRRA (siERRα), whereas ERRα overexpression employed ovERRα; PTPMT1 knockdown and overexpression were performed using LV-sh-PTPMT1 (siPTPMT1) and ovPTPMT1, respectively. Negative control vectors were obtained from GeneChem (Shanghai, China).

Animal studies and xenograft models

Female BALB/c nude mice aged 4–5 weeks were obtained from Zhejiang Weitong Lihua Experimental Animal Technology (Charles River, China). KLE cells stably transduced with ovERRα, siERRα, ovPTPMT1, siPTPMT1, or normal control vectors were injected subcutaneously into mice to establish cell line-derived xenograft (CDX) models. For treatment evaluation, KLE cells were transplanted into the axillary region of recipient mice. Mice received intraperitoneal injections of either physiological saline, carlumab (20 mg/kg), XCT790 (4 mg/kg), or a combination of carlumab (20 mg/kg) and XCT790 (4 mg/kg). Tumor dimensions were recorded every three days, and volumes were calculated using the formula: volume = (length × width²)/2. At the conclusion of the study, mice were euthanized under anesthesia, and tumors were excised for further analyses. All procedures adhered to the guidelines of the Experimental Animal Ethics Committee of Fujian Medical University (No. FJMU IACUC 2021–0451).

Patient cohort and clinical samples

A retrospective analysis was conducted on 218 patients who underwent primary hysterectomy for EC with IHC-confirmed pathology at Fujian Provincial Maternity and Children's Hospital between 2013 and 2018. Exclusion criteria included prior chemotherapy, radiotherapy, or immunotherapy (n=31), presence of additional malignancies (n=11), and insufficient tumor tissue for

pathological assessment (n=10), resulting in 166 eligible patients. Clinicopathologic and demographic data were collected from hospital records. Additionally, peripheral blood from six healthy female donors was collected to generate PBMCs for in vitro co-culture experiments with EC cells to evaluate transwell migration. The study protocol was approved by the Ethics Committee of Fujian Maternal and Child Health Hospital (No. 2023KY117).

Bioinformatics and pathway analysis

Expression levels of ESRRA, CD11b, CD68, CD80, CD86, CD115, and CD163, along with clinical data for EC patients, were retrieved from the UCSC Xena platform and The Cancer Genome Atlas (TCGA) database (https://portal.gdc.cancer.gov/) [22]. Patients were stratified into high- and low-expression groups for CD115, CD163, or ESRRA, and survival analyses were conducted. To investigate molecular networks, the top 150 genes correlated with ESRRA or PTPMT1 were identified from ARCHS4 and subjected to KEGG pathway enrichment analysis. Pathways showing overlap between ESRRA and PTPMT1 were scored, and the pathway with the highest aggregate score was selected for further study.

Quantification of cytokines by ELISA

Secreted chemokines including CCL2, fractalkine, and eotaxin were measured in EC cell culture supernatants using ELISA kits (RK00052, RK10110, RK10020; ABclonal, Wuhan, China), following manufacturer instructions. Experiments were performed in three independent replicates, with three technical repeats per experiment. Serum levels of CCL2 in treated mice were assessed similarly using an ELISA kit (RK00381; ABclonal, Wuhan, China), with five mice per group and three technical replicates per mouse.

Macrophage chemotaxis assay

THP-1 cells were first plated in the upper compartment of 6-well transwell inserts with 8 μm pores. To induce M0 macrophage differentiation, cells were treated with 100 ng/mL phorbol-12-myristate-13-acetate (PMA) for 24 hours. Concurrently, 20 mL of peripheral blood from six healthy female donors was collected in anticoagulant tubes. PBMCs were isolated using the SepMate protocol, counted, and seeded at 4×10^6 cells per well in 6-well plates. After overnight culture, the medium was replaced with RPMI-1640 supplemented with 10 percent FBS and 20 ng/mL macrophage colony-stimulating factor (M-CSF) to drive monocyte-to-macrophage differentiation, with media changes every three days. Following six days, adherent cells were confirmed as M0 macrophages. To generate polarized phenotypes, M0 macrophages were incubated with 100 ng/mL lipopolysaccharide (LPS) plus 20 ng/mL IFN-γ for 48 hours to induce M1 polarization, or with 20 ng/mL IL-4 and 20 ng/mL IL-13 for 48 hours to generate M2 macrophages. For chemotaxis assays, macrophages were plated in the upper chamber, and ECCs were seeded in the lower chamber. Co-cultures were incubated at 37°C for twenty four hours. During drug intervention experiments, ECCs were pretreated with either five mM N-acetyl-L-cysteine or five μg/mL carlumab for twenty four hours. Following incubation, non-migrated cells were removed from the upper surface, while migrated cells were fixed in 4 percent paraformaldehyde for twenty to thirty minutes, washed with PBS, stained with 0.1 percent crystal violet for five to ten minutes, rinsed, and air-dried. Five random fields were imaged and counted under an Olympus microscope. Experiments were repeated three times independently.

Cytokine profiling

Culture supernatants from ECCs (KLE-NC, KLE-ovERRα, KLE-ovPTPMT1, HEC-1A-NC, HEC-1A-ovERRα, HEC-1A-ovPTPMT1) were filtered through 0.2 μm membranes to remove debris. Samples were then processed using the Human Cytokine Antibody Array Kit (AAH-CYT-G5, RayBiotech) according to the manufacturer's instructions. Spot intensities were quantified using ImageJ software and further analyzed with RayBiotech's analytical tool (AAH-ANG-1000). Heatmaps were generated in R using the "Heatmap.2" function. Each group consisted of four technical replicates.

Intracellular reactive oxygen species (ROS) detection

Intracellular ROS levels were quantified using the DCFDA/H2DCFDA Cellular ROS Assay Kit (ab113851, Abcam, USA). ECCs from multiple experimental groups (KLE-NC, KLE-ovERRα, KLE-siERRα, KLE-ovPTPMT1, KLE-siPTPMT1, HEC-1A-NC, HEC-1A-ovERRα, HEC-1A-siERRα, HEC-1A-ovPTPMT1, HEC-1A-siPTPMT1) were analyzed using both flow cytometry (BD LSRFortessa, USA) and confocal microscopy (Leica TCS SP8, Germany). Flow cytometry was conducted in three independent experiments with three technical replicates per group. For confocal

imaging, five randomly selected fields were analyzed per group across three independent experiments.

Mitochondrial cardiolipin quantification

ECCs were stained with 45 μM 10-N-nonyl acridine orange for 15 minutes at 37°C to label cardiolipin. Cells were washed twice with 10 mM Tris/HCl (pH 7), and fluorescence was detected at 640 nm using a confocal microscope at 1,000× magnification. ImageJ was used to quantify fluorescence intensity. Five random fields per group were analyzed in three independent experiments.

Lipidomic analysis

ECCs (KLE-NC, KLE-ovERRα, KLE-ovPTPMT1, HEC-1A-NC, HEC-1A-ovERRα, HEC-1A-ovPTPMT1) were grown to 80% confluence at 1×10^5 cells/mL. Cells were washed with ice-cold PBS three times, detached with 0.25% trypsin-EDTA, and collected by centrifugation at 300×g for five minutes at 4°C. Pellets were resuspended in 1 mL ice-cold PBS, counted, and adjusted to 10^7 cells/mL. For lipid extraction, 1.5 mL of cell suspension was homogenized with 1.5 mL chloroform/methanol (2:1, v/v) containing 0.01 percent butylated hydroxytoluene. Samples were vortexed, sonicated on ice for 30 s at 30 percent amplitude, and centrifuged at 3,000 rpm for ten minutes. The organic phase was washed with 0.1 M KCl, collected, dried under nitrogen, and stored at −80°C. Before LC-MS analysis, dried samples were resuspended in 200 μL isopropanol/methanol (1:1, v/v). Quality control samples were pooled from all experimental groups. Lipidomic profiling was performed using an Agilent 1260 LC system coupled to an Agilent 6460 triple quadrupole mass spectrometer, employing multiple reaction monitoring with polarity switching. Data processing followed standard procedures provided by Shanghai Applied Protein Technology. Six biological replicates were included for each of the six experimental groups.

Tandem mass tag (TMT) proteomic analysis

Total protein was isolated from KLE cells treated with 10 μM XCT790 or vehicle for 24 hours. Protein lysates were separated by SDS-PAGE and visualized with standard staining. Proteins were enzymatically digested using sequencing-grade trypsin (Promega, USA), and resulting peptides were labeled using a TMT reagent kit (Thermo Fisher Scientific, USA). After desalting, peptide fractions were resolved via high-pH reverse-phase HPLC and subsequently analyzed by online electrospray tandem mass spectrometry. Proteins showing statistically significant fold changes were identified as differentially expressed.

Western blotting

Protein lysates from KLE and HEC-1A cells were quantified, separated, and transferred to membranes following standard protocols. Blots were probed with primary antibodies targeting ERRα (1:500, Abcam, UK), PTPMT1 (1:500, Proteintech, China), CCL2 (1:500, Abcam, UK), NF-κB p50 (1:1000, CST, USA), NF-κB p65 (1:1000, CST, USA), and GAPDH (1:2000, Immunoway, USA) as a loading control. Band intensities were quantified using ImageJ, and statistical analyses and graphical representations were performed with GraphPad Prism. Experiments were repeated three times independently.

Reverse transcription-quantitative PCR (RT-qPCR)

Following gene modulation or drug treatment, ECCs were lysed directly in culture plates for RNA extraction. Lysates were clarified by centrifugation, and the aqueous phase was collected following chloroform extraction. RNA was precipitated with isopropanol, washed with 75 percent ethanol, and reverse transcribed into cDNA using PCR Master Mix (Promega, USA). Quantitative PCR was performed with Eastep QPCR Master Mix (Promega, USA), and relative expression levels were calculated using the $2^{-\Delta\Delta Ct}$ method with GAPDH as the internal control. Each experiment included three independent replicates with three technical repeats per group.

Mitochondrial stress assay

Oxygen consumption rate (OCR) was measured using the Seahorse XF Cell Mito Stress Test Kit (Agilent Technologies, USA). Cells (KLE and HEC-1A) with various gene perturbations were plated at 4×10^4 cells per well in 24-well plates. Detection medium consisted of Seahorse XF base medium supplemented with 1 mM pyruvate, two mM glutamine, and ten mM glucose. Oligomycin, FCCP, and Rot/AA solutions were added sequentially to assess mitochondrial function. Cells were pre-incubated in CO_2-free conditions for 1 hour at 37°C, and OCR data were acquired and analyzed with the Seahorse XF24 system. Experiments were conducted in triplicate with three technical replicates each.

Transmission electron microscopy (TEM)

Cell pellets were fixed in a mixture of 2.5 percent glutaraldehyde and 2 percent paraformaldehyde in 0.1 M phosphate buffer (PB, pH 7.4) for two to four hours at 4°C. Samples were washed, embedded in 1% low-melting-point agarose, and solidified on a cold plate. Cubes (~1 mm³) were post-fixed with 1 percent osmium tetroxide for 2 hours at room temperature in the dark. Dehydration was performed through a graded ethanol series (30–100%) and two washes in acetone. Samples were infiltrated with increasing concentrations of EMbed 812 resin in acetone and polymerized at 37°C for twenty four hours, followed by 65°C for 48 hours. Ultrathin sections (60–80 nm) were cut, collected on 200-mesh copper grids, and stained with 2 percent uranyl acetate and lead citrate. Sections were examined with a JEOL JEM-1400 Plus TEM at 80 kV, and images were captured using a Gatan Orius SC1000 camera. Five random fields per sample were analyzed across three independent experiments.

Luciferase reporter assays

Potential transcriptional regulation of PTPMT1 by ESRRA was first predicted using the UCSC genome browser, and candidate binding sites were confirmed via JASPAR (https://jaspar.genereg.net/analysis). Promoter fragments of PTPMT1 of varying lengths relative to the transcription start site (PTPMT1-15: −1438 to +24, PTPMT1-16: −1123 to +24, PTPMT1-18: −724 to +24, PTPMT1-17: −549 to +24) were amplified by PCR and cloned into the pGL3-basic plasmid. Specific nucleotide sequences predicted to bind ESRRA (3′-GTTCACCCTGG-5′ and 3′-CCTGCCCTAGGACAGG-5′) were mutated to generate PTPMT1-1-MUT and PTPMT1-2-MUT constructs. HEK-293T cells were co-transfected with these plasmids in 24-well plates. After 48 hours, firefly and Renilla luciferase activities were measured using a Dual-Lite Luciferase Assay System (Promega, Beijing, China) and a microplate reader, and promoter activity was determined by the firefly/Renilla ratio.

CUT&Tag library preparation, sequencing, and analysis

CUT&Tag assays were performed following the manufacturer's protocol (Novoprotein, Jiangsu, China). Cells were immobilized on concanavalin A-coated magnetic beads and permeabilized with digitonin. pA-Tn5 transposase, guided by specific antibodies, cleaved DNA proximal to bound proteins, simultaneously ligating adapters at cleavage sites. Libraries were amplified by PCR, purified with AMPure beads, and quality-checked on an Agilent Bioanalyzer 2100. Sequencing reads were aligned to the reference genome, and ChIPseeker was used to annotate peaks and identify proximal genes for downstream analysis.

Immunohistochemistry (IHC)

For patient-based analyses, tissue sections from 166 EC cases were evaluated. Tumor samples from xenograft experiments (n=5 mice per group) were also collected following euthanasia at defined experimental endpoints. Sections were stained using antibodies against ERRα (1:100, Abcam), PTPMT1 (1:100, Proteintech), CCL2 (1:50, Abcam), CD115 (1:100, Proteintech), and CD163 (1:50, Abcam). Three random low-power fields (100×) per section were used to assess staining intensity (scored 0–3) and the proportion of positive cells (scored 1–4). Multiplying intensity by proportion yielded an overall IHC score, with 0 = negative, 1–4 = weakly positive, 5–8 = positive, and 9–12 = strongly positive. Immune cell counts were performed on five high-power fields (400×).

Multiplex immunohistochemistry (mIHC)

Paraffin-embedded tumor sections (4 μm) were processed for multiplex fluorescence staining using a TSA-based six-color system (Absin Bioscience). After deparaffinization and rehydration, antigen retrieval was conducted in citrate buffer (pH 6.0) at 90°C for 15 min using microwave irradiation. Sequential cycles of primary antibody incubation (30 min), HRP-conjugated secondary antibody application (10 min), and tyramide-fluorophore development (10 min) were performed, with microwave-mediated antibody stripping between cycles. Antibody/fluorophore pairings were: ERRα-TSA 780, PTPMT1-TSA 480, CCL2-TSA 570, CD115-TSA 620, and CD163-TSA 520; nuclei were counterstained with DAPI. Slides were mounted with antifade medium, scanned with a Pannoramic MIDI II digital slide scanner, and fluorescence intensity and cellular localization were quantified using HALO software.

Organoid culture

Fresh surgical specimens from three EC patients were thoroughly washed with DPBS containing antibiotics, finely minced using sterile scissors, and transferred into 15 mL conical tubes containing a digestion mixture composed of DMEM, collagenase, dispase, and 10 μM Y-27632. Samples were incubated at 37°C with gentle agitation until the tissue was fully dissociated. Digestion

was terminated by adding DMEM supplemented with 5% FBS, and the suspension was filtered through a 100 µm cell strainer to remove residual debris. Cell pellets were collected by centrifugation at 200×g for 5 min at 4°C, gently resuspended in organoid medium, and mixed with Matrigel at a 1:3 (v/v) ratio before seeding into pre-warmed 24-well plates. After 15–30 min incubation at 37°C to allow Matrigel polymerization, 400 µL of organoid culture medium was added per well. Medium was refreshed every 3–4 days, and organoid morphology and growth were routinely monitored. Three independent experiments per patient were conducted, each with three technical replicates.

Statistical analysis and reproducibility

Data analysis was performed using SPSS V.23.0 (IBM, Armonk, NY, USA), ImageJ, FlowJo, GraphPad Prism 8, and R software. Statistical tests applied for each dataset are specified in the respective figure legends. All experimental results represent biological replicates, with replicate numbers indicated in figure legends. Experiments were independently repeated to confirm reproducibility. Sample sizes were not predetermined by statistical methods, and no data points were excluded from analysis. Experiments were conducted without randomization, and investigators were not blinded to experimental groups or outcomes.

ERRα expression correlates with M2 macrophage infiltration and poor EC prognosis

Previous studies indicated that ERRα is closely linked to EC progression [4] and may interact with macrophages [14]. Macrophage subsets were defined using established markers: CD11b and CD68 for M0 macrophages, CD80 and CD86 for M1 macrophages, and CD115 and CD163 for M2 macrophages [23, 24]. Analysis of TCGA data revealed no significant differences in M0 or M1 macrophage abundance between early-stage (I–II) and advanced-stage (III–IV) EC tissues **(Figures 1a–1d)**. In contrast, advanced-stage EC samples displayed markedly higher M2 macrophage infiltration **(Figures 1e and 1f)**. ERRα (ESRRA) expression was significantly elevated in advanced-stage versus early-stage tumors **(Figure 1g)**. Clinically, patients with elevated M2 macrophage infiltration **(Figures 1h and 1i)** or higher ERRα levels **(Figure 1j)** exhibited worse outcomes. ERRα expression positively correlated with M2 markers CD115 and CD163, but not with M0 (CD68) or M1 (CD80, CD86) markers **(Figures 1k–1p)**.

To explore the functional link between ERRα and macrophage behavior, a co-culture system of ECCs and macrophages was established. Macrophage polarization (M0, M1, M2) was confirmed via RT-qPCR for phenotype-specific markers. Chemotaxis assays revealed that overexpression of ERRα in ECCs significantly enhanced M2 macrophage migration **(Figures 1u and 1v)**, whereas ERRα knockdown reduced it. In contrast, M0 and M1 macrophage chemotaxis remained unchanged under these conditions **(Figures 1q–t)**. Notably, co-culture with M2 macrophages did not affect ERRα protein or mRNA levels in ECCs **(Figures 1w–1y)**, suggesting that tumor-cell ERRα upregulation drives M2 macrophage recruitment rather than being a consequence of macrophage infiltration.

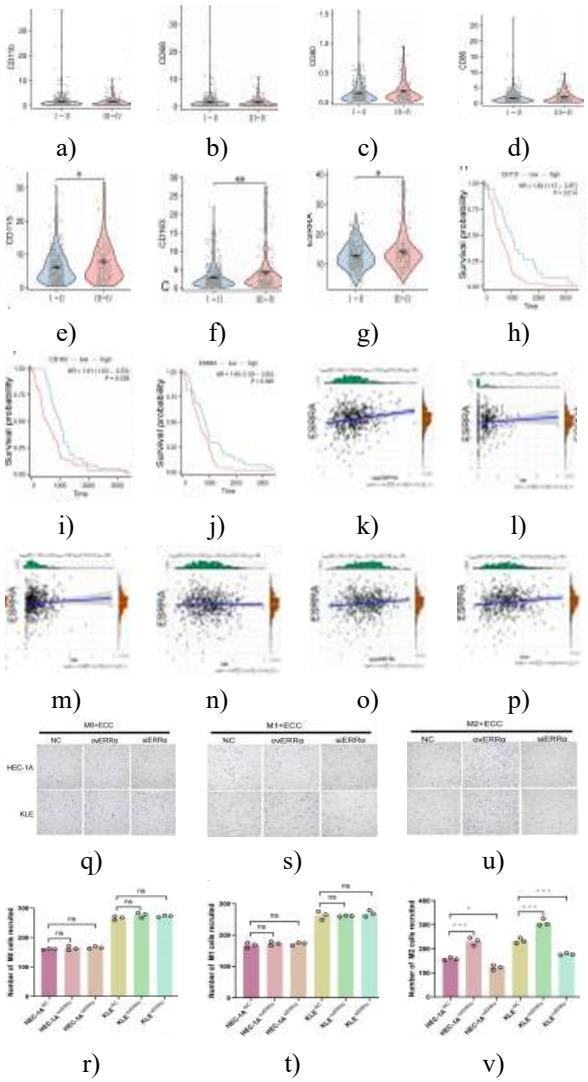

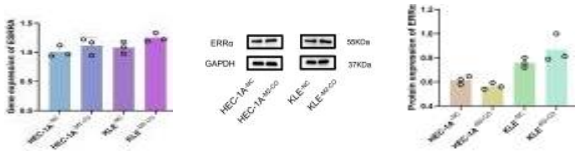

w) x) y)

Figure 1. ERRα enhances M2 macrophage infiltration and is linked to adverse prognosis in EC. (a–b) M0 macrophage abundance in early and advanced EC stages was assessed using CD11b and CD68 as markers, based on data from UCEC patients in TCGA. Statistical significance was determined using Student's t-test. The cohort included 539 patients: 339 stage I, 51 stage II, 120 stage III, and 29 stage IV. (c–d) M1 macrophages were quantified using CD80 and CD86 across different EC stages, with TCGA data analyzed via Student's t-test. (e–f) M2 macrophages were evaluated using CD115 and CD163 in patients with early or late-stage EC. (g) ERRα expression was compared between early and advanced EC, analyzed by Student's t-test. (h–j) Kaplan-Meier survival analyses for UCEC patients (TCGA cohort) stratified by CD115, CD163, and ERRα expression revealed prognostic differences, with significance determined by log-rank tests. (k–p) Correlations between ERRα and macrophage markers were visualized using scatter plots with linear regression lines and 95% confidence intervals; Pearson correlation coefficients and two-sided P values were calculated. (q–r) Representative co-culture images show how manipulating ERRα in EC cells alters M0 macrophage migration (scale bar 200 μm). Quantification represents mean±SD from three independent experiments, with five random fields analyzed per sample, using one-way ANOVA for statistics. (s–t) Migration of M1 macrophages under ERRα modulation was assessed similarly. (u–v) M2 macrophage chemotaxis in response to ERRα manipulation was quantified. (w) RT-qPCR measured ESRRA mRNA levels in EC cells after co-culture with M2 macrophages; results are mean±SD from three independent experiments with three technical replicates, analyzed with Student's t-test. (x–y) Western blotting of ERRα protein expression in the same co-culture conditions was performed in parallel, with GAPDH as a loading control; data are mean±SD from three independent experiments, analyzed with Student's t-test. ns, not significant; *p<0.05, **p<0.01, ***p<0.001. ANOVA= analysis of variance; EC= endometrial cancer; ERRα= estrogen-related receptor α; TCGA= The Cancer Genome Atlas; RT-qPCR= reverse transcription-quantitative polymerase chain reaction.

PTPMT1 is a critical ERRα target mediating M2 macrophage chemotaxis

To investigate how ERRα drives M2 macrophage recruitment, quantitative proteomics was conducted in KLE EC cells. Proteins with p<0.1 and fold change >1.3 (upregulated) or <0.7 (downregulated) were considered significant. Fourteen proteins were differentially expressed, including five upregulated (DDRGK1, TXNDC12, IFRD1, RSRC2, APLP2) and nine downregulated (MRPS2, UCK2, PTPMT1, NUCB1, KIF20A, PPL, HMGCS1, ACSS2, S100A6). Given ERRα's role in mitochondrial metabolism [5], PTPMT1—known to regulate mitochondrial morphology and cardiolipin biosynthesis [7]—was prioritized for further study **(Figure 2a)**. Overexpression of ERRα (ovERRα) increased PTPMT1 mRNA and protein levels, whereas ERRα knockdown (siERRα) reduced them; altering PTPMT1 did not impact ERRα expression **(Figures 2b–2f)**. Dual-luciferase reporter assays pinpointed the ERRα binding region in the PTPMT1 promoter between −724 bp and −549 bp **(Figures 2g and 2h)**. Mutational analysis of two candidate sites identified a functional binding site at −624 bp to −609 bp, with consensus sequence CCTGCCCTAGGACAGG **(Figures 2i and 2j)**. ChIP-seq further validated direct ERRα binding at this promoter region **(Figures 2k and 2l)**. Functionally, in a co-culture system with M2 macrophages, PTPMT1 overexpression enhanced macrophage chemotaxis, while PTPMT1 knockdown reduced it. Importantly, the chemotactic effect driven by ERRα overexpression was partially reversed by PTPMT1 silencing, confirming PTPMT1 as a key mediator of ERRα-induced M2 macrophage recruitment **(Figures 2m and 2n)**.

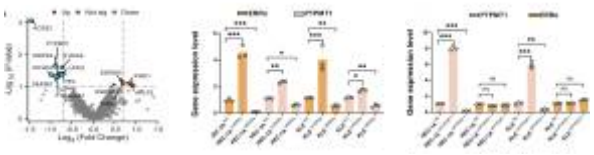

a) b) c)

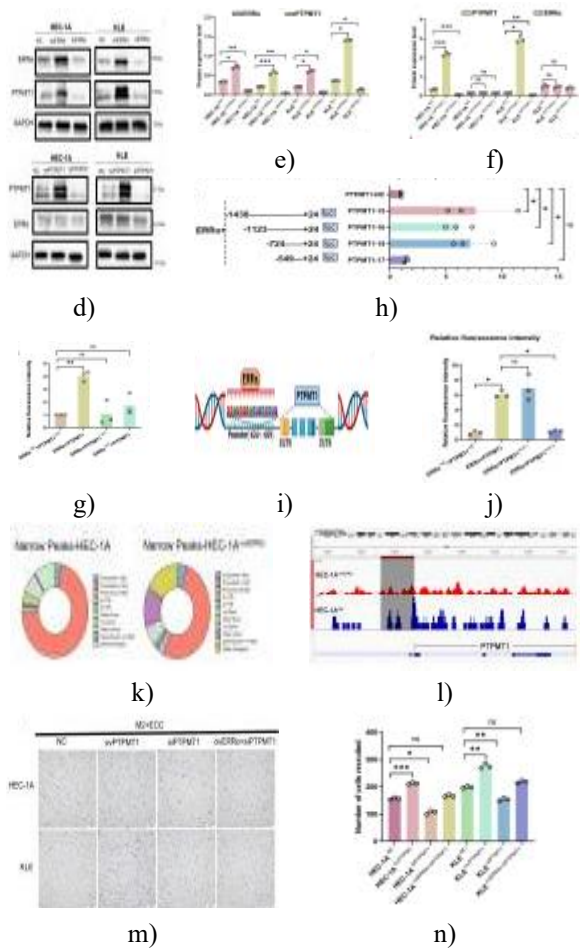

Figure 2. ERRα controls PTPMT1 to drive M2 macrophage migration. (a) Proteomic profiling followed by hierarchical clustering identified proteins associated with ERRα, with volcano plots highlighting 14 significantly correlated candidates; PTPMT1 was the protein most directly linked to mitochondrial metabolic regulation. (b–c) RT-qPCR was used to quantify ERRα and PTPMT1 expression in ECCs under normal control (NC), ERRα overexpression (ovERRα), or ERRα knockdown (siERRα) conditions. GAPDH served as a loading control. Data are presented as mean±SD from 3 independent experiments, with statistical comparisons via one-way ANOVA. (d–f) Western blot analysis of ERRα and PTPMT1 protein levels in ECCs after PTPMT1 overexpression (ovPTPMT1) or knockdown (siPTPMT1) compared with NC, using GAPDH as a loading control; results are mean±SD from three independent experiments, analyzed with one-way ANOVA. (g–h) Dual-luciferase reporter assays mapped the ERRα-responsive region of the PTPMT1 promoter between −724 bp and −549 bp. Four promoter fragments (PTPMT1-15: −1438 to +24, PTPMT1-16: −1123 to +24, PTPMT1-18: −724 to +24, PTPMT1-17: −549 to +24) were cloned into pGL3-basic and co-transfected with ERRα; luciferase activity was normalized to Renilla luciferase at 48 h post-transfection. Data are mean±SD from three independent experiments, analyzed with one-way ANOVA. (i–j) Mutational analysis of the PTPMT1 promoter (PTPMT1-mut-1, PTPMT1-mut-2, and wild-type) co-transfected with ERRα confirmed the functional ERRα binding site at −624 bp to −609 bp (consensus: CCTGCCCTAGGACAGG). Data are mean±SD from three independent experiments; significance was evaluated by one-way ANOVA. (k) CUT&Tag combined with sequencing illustrated the genomic distribution of ERRα binding peaks in functional gene regions. (l) Occupancy of the PTPMT1 promoter by ERRα was validated in HEC-1A cells. (m–n) M2 macrophage migration in response to PTPMT1 modulation was assessed in a co-culture model (scale bar 200 μm); five random fields per sample were analyzed, and data are mean±SD from three independent experiments. Statistical significance was determined by one-way ANOVA. ns, not significant; *p<0.05, **p<0.01, ***p<0.001. ANOVA= analysis of variance; ECC= endometrial cancer cell; ERRα= estrogen-related receptor α; NC= normal control; PTPMT1= protein tyrosine phosphatase mitochondrial 1; RT-qPCR= reverse transcription-quantitative polymerase chain reaction.

ERRα–PTPMT1 axis enhances mitochondrial OXPHOS and recruits M2 macrophages via ROS signaling

To investigate the downstream mechanism of ERRα/PTPMT1-mediated M2 chemotaxis, the top 150 genes associated with ESRRA or PTPMT1 were identified using Spearman correlation analysis on integrated RNA-seq and ChIP-seq datasets. KEGG pathway analysis via the ARCHS4 signature search revealed oxidative phosphorylation (OXPHOS) as the top enriched pathway (excluding disease-related terms) for both gene sets **(Figures 3a and 3b)**, prompting further focus on OXPHOS. ECCs with ERRα or PTPMT1 overexpression or knockdown were subjected to mitochondrial stress assays using the Seahorse XF24 analyzer. Overexpression of either ERRα or PTPMT1 significantly increased basal respiration, ATP

production, maximal respiration, and spare respiratory capacity, whereas knockdown of either gene reduced these parameters **(Figures 3c–3f)**. Importantly, the ovERRα+siPTPMT1 condition abolished the ERRα-driven increases in respiratory function, indicating that PTPMT1 is essential for ERRα-mediated mitochondrial OXPHOS activation.

Because mitochondrial OXPHOS is a major ROS source, ROS levels were measured by flow cytometry and confocal microscopy in KLE and HEC-1A cells. ERRα or PTPMT1 overexpression led to markedly elevated ROS, while knockdown reduced ROS production **(Figures 3g–3p)**. To determine whether ROS mediates M2 macrophage recruitment, ECC–M2 co-culture experiments were conducted with the ROS scavenger N-acetylcysteine (NAC). NAC treatment significantly suppressed M2 migration in NC (NC+NAC) as well as in ERRα or PTPMT1 overexpressing ECCs (ovERRα+NAC, ovPTPMT1+NAC) compared with untreated controls **(Figures 3q–3r)**. These findings demonstrate that the ERRα–PTPMT1 axis promotes M2 macrophage chemotaxis through an ROS-dependent mechanism.

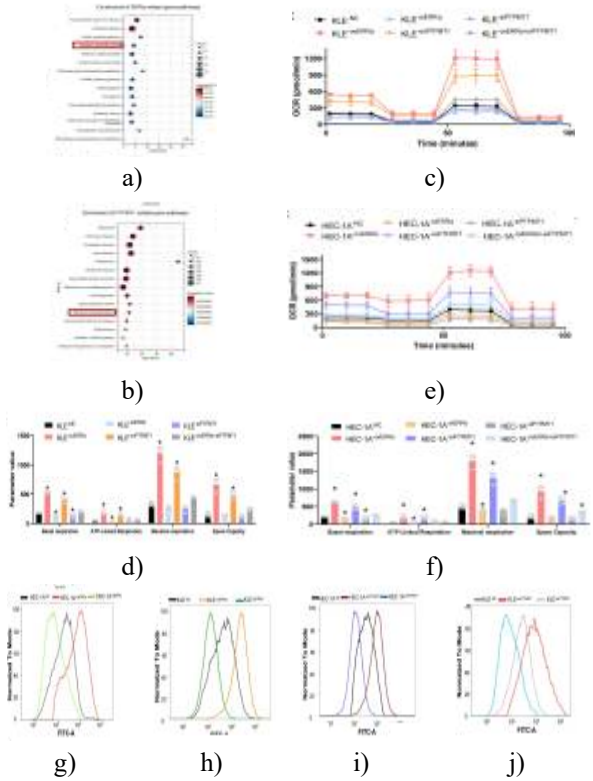

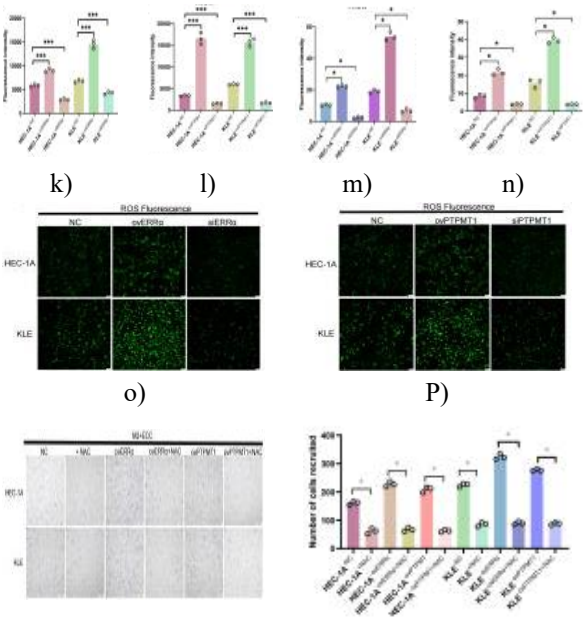

Figure 3. The signaling pathway involving ERRα and PTPMT1 enhances the infiltration of M2-type macrophages through reactive oxygen species (ROS)-mediated stimulation of mitochondrial oxidative phosphorylation (OXPHOS). (a–b) Computational pathway enrichment analysis identified common biological processes linked to ERRα and PTPMT1 expression. Oxidative phosphorylation emerged with the strongest enrichment score among the leading 15 non-disease-related pathways for each factor. (c–f) Measurements of oxygen consumption rate (OCR) via Seahorse assay illustrated the impact of the ERRα-PTPMT1 pathway on key mitochondrial parameters, including baseline respiration, maximum respiratory capacity, reserve capacity, and ATP-linked production. Control conditions involved KLE and HEC-1A cells with normal expression (NC). Results are presented as mean ± standard deviation from three separate experiments, each with triplicate measurements. Statistical comparisons used one-way analysis of variance. (g–l) Flow cytometry quantification of intracellular ROS in cells with altered ERRα or PTPMT1 levels. NC groups from KLE and HEC-1A lines served as references. Data represent mean ± standard deviation across three independent runs with technical triplicates. One-way ANOVA was applied for significance testing. (m–p) Confocal microscopy assessment of ROS accumulation in various ERRα/PTPMT1-modified groups. Controls were KLE-NC and HEC-1A-NC

cells. Values shown are mean ± standard deviation, based on analysis of five random fields per group over three experiments. One-way ANOVA determined p-values. (q–r) Influence of ROS generated by endometrial cancer cells on the migration of M2 macrophages in a transwell co-culture system (scale bar: 200 µm). Data are mean ± standard deviation from three experiments, with cell counts from five fields each. Student's t-test was used (*p < 0.05, ***p < 0.001). Abbreviations: ANOVA, analysis of variance; ECC, endometrial carcinoma cell; ERRα, estrogen-related receptor alpha; CL, cardiolipin; NAC, N-acetylcysteine; NC, negative control; PG, phosphatidylglycerol; PTPMT1, protein tyrosine phosphatase mitochondrial 1; ROS, reactive oxygen species.

Partial dependence of ERRα-driven cardiolipin elevation on PTPMT1

To examine how ERRα influences cardiolipin (CL) abundance—a critical phospholipid for mitochondrial integrity and activity [25]—we performed comprehensive lipid profiling in endometrial carcinoma lines across multiple conditions: KLE and HEC-1A cells with baseline expression (NC), ERRα overexpression (ovERRα), or PTPMT1 overexpression (ovPTPMT1). In total, 48 distinct lipid species were quantified **(Figure 4a)**. Results indicated markedly higher CL content in both cell lines following elevated ERRα or PTPMT1 **(Figure 4b)**. In HEC-1A-ovERRα cells, the most prominent rises occurred in CL (14:0/18:0/14:0/18:2) and CL (16:0/16:0/16:0/16:0), with similar increases in the PTPMT1-overexpressing counterparts **(Figures 4c and 4d)**. For KLE cells, ovERRα led to enrichment of CL (14:0/18:0/14:0/18:2) and CL (14:0/18:2/16:0/18:1), while ovPTPMT1 boosted CL (14:0/18:0/16:0/18:1) and CL (16:0/16:0/16:0/16:0) **(Figures 4e and 4f)**. Two specific CL variants, CL (14:0/16:0/18:0/18:2) and CL (14:0/16:0/16:0/18:1), were consistently upregulated in all overexpression groups relative to controls **(Figure 4g)**. Given PTPMT1's role in converting phosphatidylglycerol phosphate (PGP) to phosphatidylglycerol (PG) via dephosphorylation [26], PG concentrations were also found to be substantially higher in cells with increased ERRα or PTPMT1 compared to NC **(Figure 4h)**. Moreover, a strong positive association emerged between PG and CL quantities in both cell lines across all conditions **(Figure 4i)**.

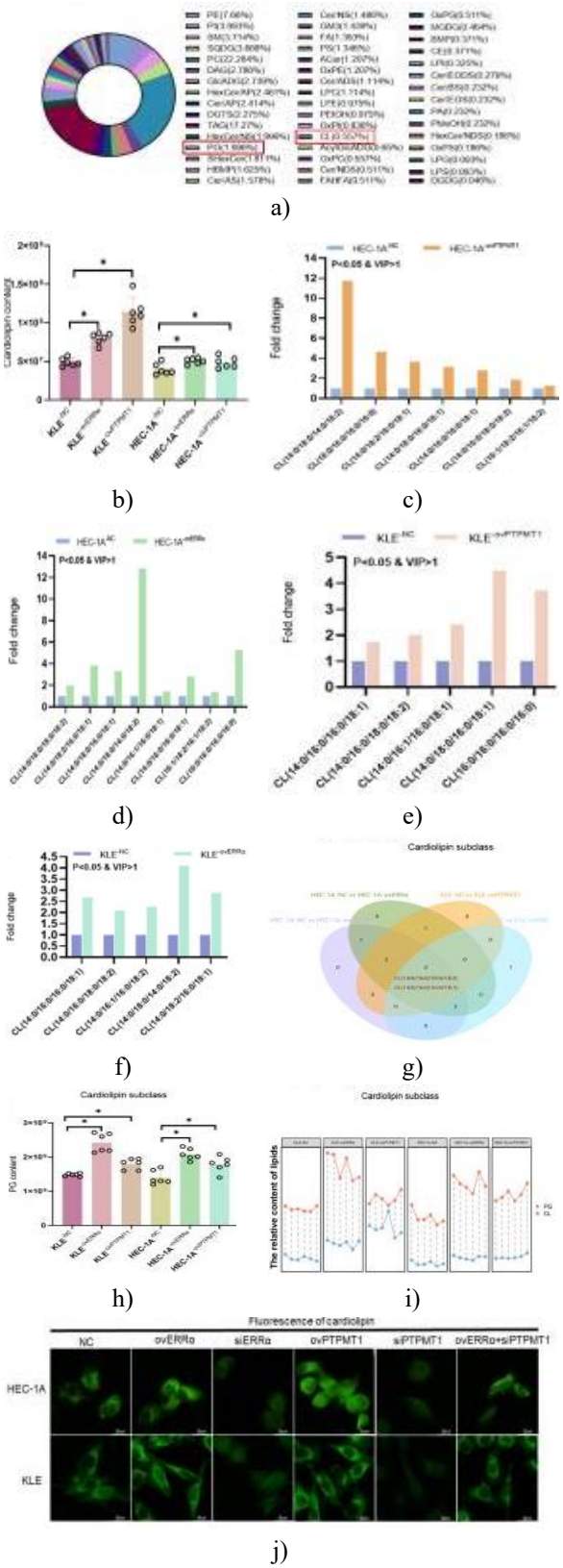

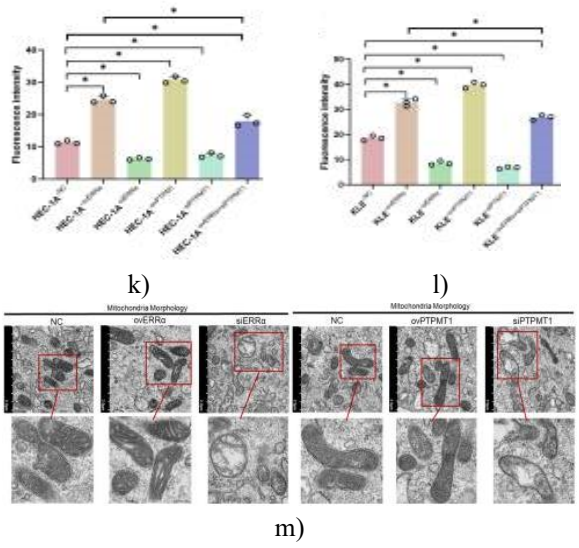

Figure 4. The ERRα-PTPMT1 pathway influences cardiolipin abundance and mitochondrial architecture. (a) Lipidomic profiling identified 36 distinct lipid classes in both KLE and HEC-1A endometrial cancer cell lines. (b) Quantification of total cardiolipin (CL) across various ERRα and PTPMT1 modulation groups via lipidomics, with KLE-NC and HEC-1A-NC serving as baseline controls. Six biological replicates were included per group, and one-way ANOVA was used for statistical analysis. (c–f) Differential analysis of specific CL subclasses in ERRα/PTPMT1-altered groups, highlighting species with fold change >1.2, $p<0.05$, and VIP>1. Controls were KLE-NC and HEC-1A-NC cells. (g) Venn diagram illustrating overlap, where two CL species—CL (14:0/16:0/18:0/18:2) and CL (14:0/16:0/16:0/18:1)—were consistently upregulated in all overexpression conditions (ERRα or PTPMT1) relative to untreated controls. (h) Assessment of phosphatidylglycerol (PG) levels in ERRα/PTPMT1-modified groups by lipidomics, using KLE-NC and HEC-1A-NC as controls. Six technical replicates per group; one-way ANOVA for p-values. (i) Illustrative summary depicting the association between CL and PG contents across tested conditions, based on six technical replicates per group. (j–l) Staining of mitochondrial CL using 10-N-nonyl acridine orange, followed by confocal imaging (scale bar: 20 μm). Fluorescence signals were quantified with ImageJ software. Results are mean ± standard deviation from three independent experiments, analyzing five random fields each. One-way ANOVA applied for significance. (m) Transmission electron microscopy evaluation of mitochondrial ultrastructure in ERRα/PTPMT1-altered groups (scale bar: 2 μm). Five fields per group were examined across three experiments. *$p<0.05$. Abbreviations: ANOVA, analysis of variance; ERRα, estrogen-related receptor alpha; CL, cardiolipin; NC, negative control; PG, phosphatidylglycerol; PTPMT1, protein tyrosine phosphatase mitochondrial 1.

Staining specific for CL with 10-N-nonyl acridine orange, combined with confocal microscopy, demonstrated substantially stronger fluorescence in endometrial carcinoma cells (ECCs) with ERRα overexpression (ovERRα) or PTPMT1 overexpression (ovPTPMT1), whereas knockdown of ERRα (siERRα) or PTPMT1 (siPTPMT1) led to notably weaker signals. In cells combining ERRα overexpression with PTPMT1 knockdown (ovERRα+siPTPMT1), CL-associated fluorescence was still elevated above negative control levels but considerably lower than in the ovERRα-alone condition **(Figures 4j–4l)**. These findings suggest that PTPMT1 partially mediates the ERRα-induced enhancement of CL production.

Beyond functional impacts, alterations in CL content also alter mitochondrial shape [25]. Transmission electron microscopy (TEM) of HEC-1A cells showed that ovERRα or ovPTPMT1 conditions preserved well-defined inner mitochondrial membranes and prominent cristae compared to controls. Conversely, siERRα or siPTPMT1 cells displayed degraded membranes, vacuolization, and fragmented cristae **(Figure 4m)**. Such structural defects likely stem from diminished CL synthesis in the inner membrane following ERRα or PTPMT1 downregulation, compromising cristae stability and leading to morphological and functional mitochondrial impairments [25].

ERRα-PTPMT1-driven ROS stimulates CCL2 release through NF-κB activation

To elucidate how the ERRα/PTPMT1 axis controls macrophage recruitment, cytokine profiling was conducted via microarray in ovERRα, ovPTPMT1, and control (NC) endometrial cancer cells from KLE and HEC-1A lines. Three cytokines—fractalkine, eotaxin, and CCL2—showed marked upregulation in both overexpression groups relative to NC **(Figures 5a and 5b)**. Follow-up ELISA validation across all groups confirmed elevated CCL2 protein in ovERRα and

ovPTPMT1 conditions **(Figures 5c and 5d)**, while fractalkine and eotaxin remained unchanged (data not shown). Treatment with the ROS scavenger NAC substantially lowered CCL2 secretion in NC+NAC, ovERRα+NAC, and ovPTPMT1+NAC groups compared to untreated counterparts **(Figures 5e and 5f)**. Given the absence of direct ERRα binding sites in the CCL2 promoter, these observations point to indirect regulation of CCL2 via ROS. In ECC-M2 macrophage co-cultures, neutralizing CCL2 with carlumab markedly impaired M2 migration in NC+carlumab, ovERRα+carlumab, and ovPTPMT1+carlumab conditions versus untreated controls **(Figures 5g and 5h)**, underscoring CCL2's critical involvement in driving M2 macrophage attraction in endometrial cancer.

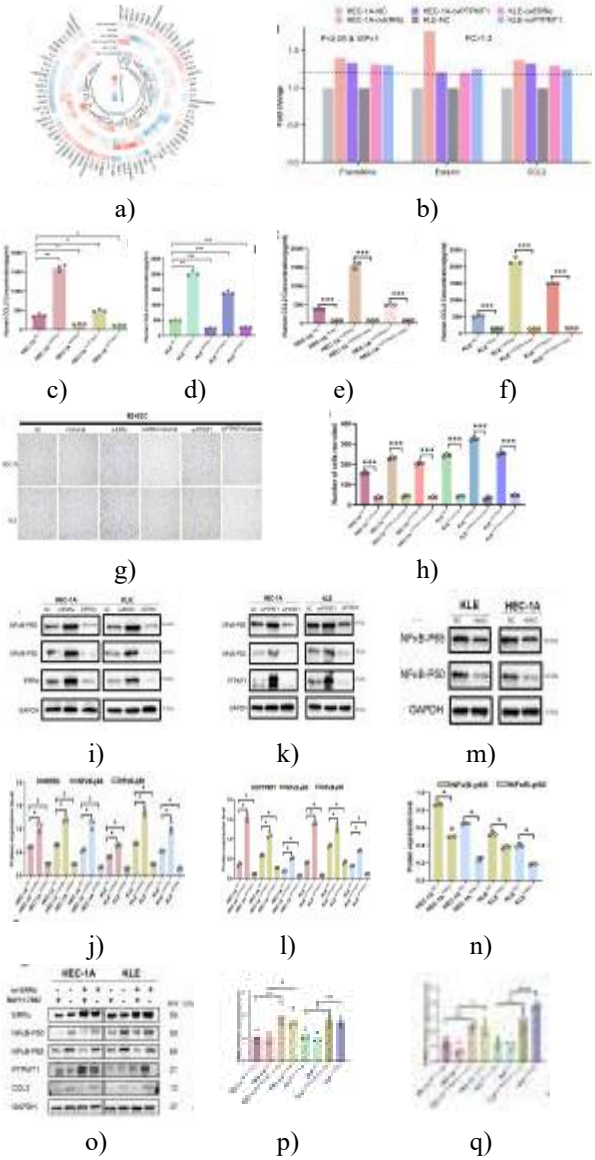

a) b) c) d) e) f) g) h) i) k) m) j) l) n) o) p) q)

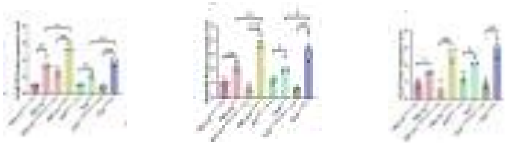

r) s) t)

Figure 5. Reactive oxygen species facilitate CCL2 release through activation of the NF-κB signaling cascade. (a) Screening of 80 cytokines using a human cytokine antibody array in cells with modulated ERRα/PTPMT1 levels. Four technical replicates were used per group. (b) Identification of three cytokines—fractalkine, eotaxin, and CCL2—with substantial upregulation in ovERRα and ovPTPMT1 conditions compared to negative controls (fold change >1.2, $p<0.05$, VIP>1). (c–d) Quantification of CCL2 protein via Human CCL2 FAST ELISA across various ERRα/PTPMT1 alteration groups. Results presented as mean ± standard deviation from three independent experiments, each with triplicate measurements. One-way ANOVA for statistical analysis. (e–f) Assessment of ROS impact on CCL2 secretion using Human CCL2 FAST ELISA. Data shown as mean ± standard deviation based on three experiments with technical triplicates. Student's t-test applied. (g–h) Influence of CCL2 from endometrial cancer cells on M2 macrophage migration in a co-culture setup. Mean ± standard deviation from three experiments; five random fields counted per condition (scale bar: 200 μm). Student's t-test for p-values. (i–l) Western blotting for NF-κB p65 and p50 subunits in endometrial carcinoma cells from NC, ovERRα, siERRα, ovPTPMT1, and siPTPMT1 groups. GAPDH as loading control. Representative blots from three experiments; one-way ANOVA for significance. (m–n) Western blot evaluation of NF-κB p65 and p50 in cells with or without NAC treatment. GAPDH loading control; three independent experiments; Student's t-test. (o–t) Western blotting demonstrated marked downregulation of CCL2 following NF-κB blockade. Representative results from three experiments; one-way ANOVA. *$p<0.05$, **$p<0.01$, ***$p<0.001$. Abbreviations: ANOVA, analysis of variance; ECC, endometrial carcinoma cell; ERRα, estrogen-related receptor alpha; NAC, N-acetylcysteine; NC, negative control; PTPMT1, protein tyrosine phosphatase mitochondrial 1.

Prior work has established that ROS can drive CCL2 production via NF-κB activation [27]. Western blot results indicated elevated NF-κB (p65 and p50) protein in ovERRα and ovPTPMT1 cells, with reduced levels in siERRα and siPTPMT1 conditions relative to controls **(Figures 5i–5l)**. Notably, NAC-mediated ROS clearance in control cells led to lower NF-κB expression **(Figures 5m and 5n)**. Furthermore, 24-hour exposure to 10 μM BAY11-7082 (an NF-κB inhibitor) substantially suppressed CCL2 levels **(Figures 5o–5t)**. Collectively, these observations imply that the ERRα-PTPMT1 axis boosts ROS, which in turn activates NF-κB to enhance CCL2 secretion.

Synergistic inhibition of tumor growth and progression by combining carlumab and XCT790

Using an established KLE cell-derived xenograft (CDX) model in mice [28], we developed variants with lentiviral-mediated modulation: CDX-ovERRα, CDX-siERRα, CDX-ovPTPMT1, and CDX-siPTPMT1, followed by subcutaneous implantation in nude mice to assess tumor formation. Mice were euthanized upon significant tumor volume differences, with tissues and serum collected for analysis (day 27 for gene-modulation studies; day 29 for drug interventions; day 0 defined as implantation). Tumors from CDX-ovERRα and CDX-ovPTPMT1 groups grew faster and reached larger volumes than controls, while CDX-siERRα and CDX-siPTPMT1 exhibited slower growth and smaller sizes **(Figures 6a and 6b)**. Immunohistochemistry on paraffin sections showed higher ERRα, PTPMT1, and CCL2 staining, along with increased M2 macrophage markers (CD163 and CD115) in overexpression groups versus controls **(Figures 6c–6g).**

For therapeutic evaluation, KLE-NC cells were implanted subcutaneously in nude mice. Monotherapy with XCT790 (ERRα antagonist) or carlumab (CCL2-neutralizing antibody) notably suppressed tumor volume **(Figures 6h and 6i)**, reduced CCL2 expression, and lessened M2 infiltration (CD115 and CD163) compared to untreated controls **(Figures 6j–6n)**. Serum CCL2 was also lower in both single-agent groups **(Figure 6o)**. The combination of carlumab and XCT790 yielded the most potent effects, producing the smallest tumors, minimal CCL2 levels, lowest M2 macrophage presence (CD115 and CD163), and greatest serum CCL2 reduction across all treatment arms.

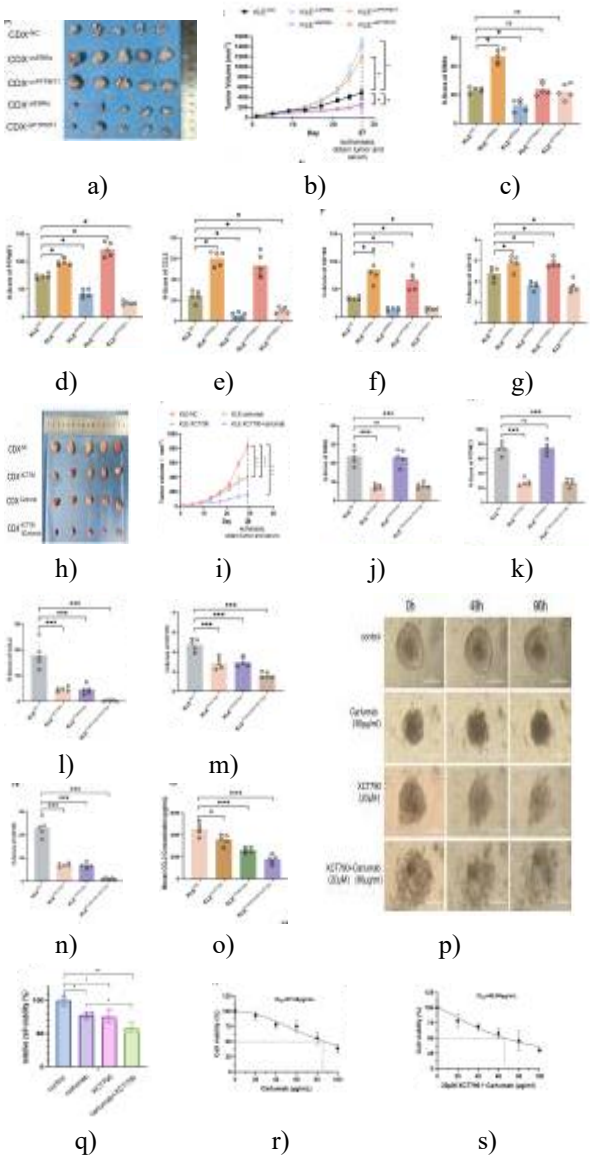

Figure 6. Co-administration of carlumab and XCT790 restrains tumor development and advancement. (a–b) Photographs of excised tumors at study endpoint and growth curves of tumor volume in BALB/c nude mice across ERRα/PTPMT1-modulated groups (day 0: cell implantation date). CDX-NC as reference control; n=5 animals/group. One-way ANOVA for statistics. (c–g) Immunofluorescence detection of ERRα, PTPMT1, CCL2, CD163, and CD115 protein in tumor samples from various ERRα/PTPMT1 groups; n=5/group. One-way ANOVA applied. (h–i) Endpoint tumor images and volume trajectories in BALB/c nude mice across four treatment arms (day 0: implantation). CDX-NC control; n=5/group. One-way ANOVA. (j–

n) Immunofluorescence quantification of ERRα, PTPMT1, CCL2, CD115, and CD163 in tumors from the treatment groups; n=5/group. One-way ANOVA. (o) Serum CCL2 concentrations via ELISA in the four groups. Mean ± standard deviation; CDX-NC control; n=5/group. One-way ANOVA. (p) Microscopic recording of organoid morphology under different treatments. Scale bar: 100 µm. (q) Cell Titer-Glo assay for viability post-treatment. DMSO-treated as control. Mean ± standard deviation from three experiments with triplicates each. One-way ANOVA. (r–s) IC50 values for carlumab and modulation by XCT790. ns, not significant; *p<0.05, **p<0.01, ***p<0.001. Abbreviations: ANOVA, analysis of variance; CDX, cell-derived xenograft; ERRα, estrogen-related receptor alpha; NC, negative control; PTPMT1, protein tyrosine phosphatase mitochondrial 1; DMSO, dimethyl sulfoxide; IC50, half-maximal inhibitory concentration.

For closer simulation of physiological conditions, endometrial cancer-derived organoids were generated to test therapeutic responses. Treatments included carlumab (80 µg/mL), XCT790 (20 µM), or their combination (80 µg/mL carlumab + 20 µM XCT790). Microscopy showed that single-agent exposure to either drug caused notable organoid contraction relative to untreated controls. The dual regimen induced not only shrinkage but also evident apoptotic features and vacuolated structures **(Figure 6p)**. Viability assays indicated reduced survival: 77.65% with carlumab alone, 75.19% with XCT790 alone, and markedly lower at 57.99% for the combination **(Figure 6q)**. Moreover, adding 20 µM XCT790 lowered the carlumab IC50 from 87.05 µg/mL to 65.99 µg/mL **(Figures 6r and 6s)**, demonstrating that ERRα blockade sensitizes organoids to CCL2-targeted therapy.

Clinical relevance of ERRα-PTPMT1-M2 macrophage axis to endometrial cancer progression

The study encompassed 166 endometrial cancer (EC) patients. Cases were stratified by FIGO stage: early (I–II) versus advanced (III–IV). Advanced-stage patients displayed higher serum CA125 and tissue Ki67 levels, validating these as reliable progression markers. Immunohistochemistry (IHC) on tumor cores assessed ERRα, PTPMT1, CCL2, and M2 markers (CD115, CD163) **(Figure 7a)**. Advanced tumors exhibited substantially elevated ERRα, PTPMT1, CCL2, and M2 macrophage density compared to early-stage **(Figures 7b–7f)**. High ERRα expressors showed greater advanced-stage prevalence and Ki67 positivity, alongside upregulated PTPMT1, CCL2, and M2 infiltration **(Figures 7g–7k)**. At the invasive margin, high ERRα correlated with increased CCL2 and M2 presence **(Figures 7l–7o)**. Multiplex IHC (mIHC) on age- and BMI-matched subsets (five early-stage vs. eight advanced-stage) confirmed denser M2 infiltration in advanced cases **(Figure 7p)**, with stronger signals for ERRα, PTPMT1, CCL2, and double-positive CD115+/CD163+ cells **(Figure 7q)**. Correlations were strong: ERRα with PTPMT1 (R^2=0.81, p<0.0001), CCL2 (R^2=0.44, p=0.0139), and M2 cells (R^2=0.70, p=0.0003); PTPMT1 with CCL2 (R^2=0.50, p=0.0068) and M2 (R^2=0.56, p=0.0032). Additionally, vimentin was higher in advanced tumors. Co-culture of human PBMC-derived M2 macrophages with modulated ECCs revealed enhanced migration toward ovERRα or ovPTPMT1 cells, while siERRα or siPTPMT1 reduced attraction **(Figures 7r–7t)**. Thus, elevated ERRα/PTPMT1 in cancer cells likely drives CCL2-mediated M2 recruitment to promote EC advancement.

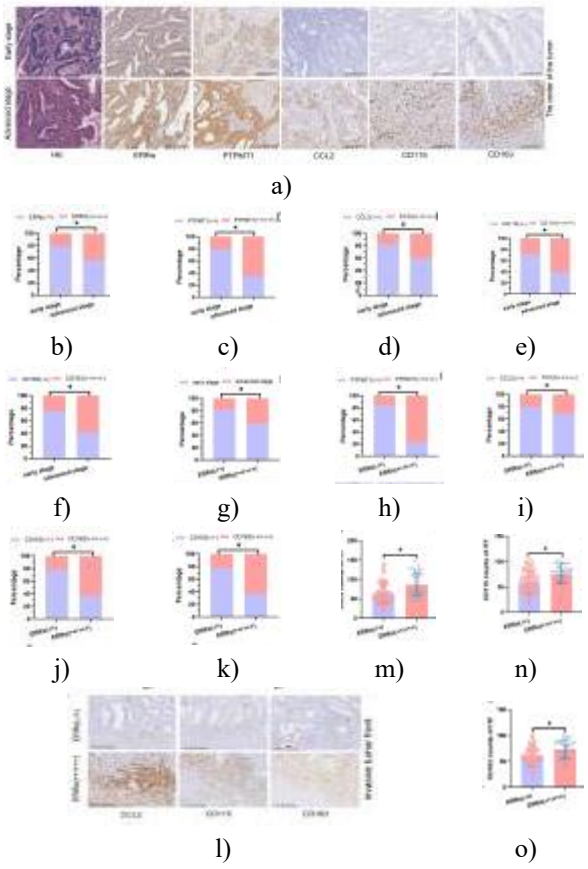

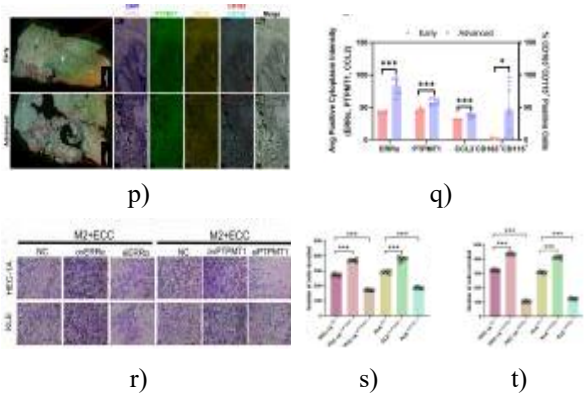

p) q)

r) s) t)

Figure 7. Expression patterns of ERRα-PTPMT1 and M2 macrophage markers in clinical endometrial cancer specimens. (a) Illustrative IHC images depicting ERRα, PTPMT1, CCL2, CD115, and CD163 in tumor tissues from early-stage (125 cases) versus advanced-stage (41 cases) EC patients (scale bar: 200 μm). (b–f) Quantification of ERRα, PTPMT1, CCL2, CD115, and CD163 levels in tumor cores of early- versus advanced-stage EC, expressed as percentages. Pearson's χ^2 test for significance. (g–k) Levels of PTPMT1, CCL2, CD115, and CD163 at the invasive margins in EC patients stratified by ERRα expression (ERRα (±): 122 cases; ERRα (++/+++): 44 cases), shown as percentages. Pearson's χ^2 test applied. (l) Representative IHC staining for CCL2, CD115, and CD163 at the invasive front in tumors with varying ERRα levels (scale bar: 200 μm). (m–o) Expression of CCL2, CD115, and CD163 at invasive margins across ERRα-stratified groups. Mean ± standard deviation; Student's t-test. (p) Multiplex IHC images highlighting M2 macrophages (CD115+CD163+), ERRα, PTPMT1, and CCL2 in early-stage (five patients) and advanced-stage (eight patients) EC tumors (scale bar: 100 μm). (q) Quantification of M2 macrophages (CD115+CD163+), ERRα, PTPMT1, and CCL2 signals in early- (5 cases) versus advanced-stage (8 cases) samples. Mean ± standard deviation; Student's t-test. (r–t) Assessment of ERRα-PTPMT1 axis influence on M2 macrophage (derived from peripheral blood mononuclear cells of six female donors) migration in co-culture assays. Results from three independent experiments, with five random fields counted each. Mean ± standard deviation; one-way ANOVA. Abbreviations: EC, endometrial carcinoma; ECC, endometrial carcinoma cell; ERRα, estrogen-related receptor alpha; NC, negative control; PTPMT1, protein tyrosine phosphatase mitochondrial 1.

Cancer cells reprogram energy metabolism to support rapid proliferation and heightened bioenergetic needs [29]. Such metabolic shifts also reshape the tumor microenvironment, facilitating immune evasion [30]. Therapies directed at metabolic pathways can exert direct cytotoxicity or enhance anti-tumor immunity [31, 32]. ERRα emerges as a key regulator linking metabolism and immune responses [14]. The ERRα-PTPMT1 pathway stimulates mitochondrial oxidative phosphorylation via elevated cardiolipin biosynthesis and subsequent ROS generation. This cascade amplifies CCL2 release from endometrial carcinoma cells, driving M2 macrophage infiltration and accelerating disease progression. Concurrent targeting of ERRα and CCL2 disrupts this recruitment and curbs tumor advancement.

As a transcriptional regulator, ERRα promotes mitochondrial oxidative phosphorylation [33]. Prior work has linked ERRα to endometrial cancer progression, emphasizing its role in lipid metabolic reprogramming tied to mitochondrial activity [4]. Cardiolipins, predominantly localized to the inner mitochondrial membrane, are essential for efficient electron transport during OXPHOS [34]. PTPMT1 facilitates cardiolipin production by dephosphorylating phosphatidylglycerol phosphate to phosphatidylglycerol [26]. Our data demonstrate a positive association between ERRα/PTPMT1 and both cardiolipin levels and OXPHOS activity, with ERRα directly enhancing PTPMT1 transcription.

Elevated CCL2 is frequently observed across malignancies, including prostate, colorectal, and breast cancers, where it fosters malignant behavior by attracting monocytes that differentiate into macrophages within the tumor microenvironment [35, 36]. In endometrial cancer, CCL2 is overexpressed relative to normal endometrium [37], with higher levels in high-grade versus low-grade tumors, promoting progression through macrophage recruitment [38]. Here, cytokine arrays and ELISA confirmed robust CCL2 upregulation in ERRα- or PTPMT1-overexpressing cells. Blocking CCL2 with carlumab markedly impaired M2 migration, implicating CCL2 as the primary chemokine modulated by the ERRα-PTPMT1 axis via enhanced OXPHOS and ROS. This aligns with evidence that ROS-induced oxidative stress alters cytokine profiles, including IL-6 and CCL2,

effects reversible by scavengers like NAC [39]. ROS also activates NF-κB to boost CCL2 transcription [27, 40].

Heightened CCL2 initiates a feed-forward loop: tumor-derived CCL2 recruits monocytes that polarize into M2-like tumor-associated macrophages, which in turn secrete additional CCL2, amplifying immunosuppression and progression [41, 42]. Clinically, advanced-stage endometrial cancer exhibited greater ERRα, PTPMT1, CCL2, and M2 marker (CD115/CD163) expression than early-stage disease. High ERRα tumors showed enriched CCL2 and M2 accumulation, particularly at invasive fronts, with macrophages clustering from periphery inward. Thus, ERRα-driven CCL2 secretion appears to orchestrate M2 infiltration into tumor regions, fueling advancement.

Overall, metabolic reprogramming in cancer cells influences cytokine output, which modulates immune components in the tumor microenvironment. This study establishes a mechanistic connection between tumor energetics and immunosuppression in endometrial cancer.

CCL2 contributes to tumorigenesis by attracting tumor-associated macrophages (TAMs), positioning it as a promising therapeutic candidate. Preclinical models employing CCL2-neutralizing antibodies or inhibitors of C-C motif chemokine receptor 2 (CCR2)—the primary CCL2 receptor—have demonstrated effective suppression of tumor expansion and spread in various malignancies, including breast [43, 44], prostate [45], liver [46], and colorectal cancers [47]. In our xenograft experiments with tumor-bearing nude mice, monotherapy using carlumab (anti-CCL2) or XCT790 (ERRα antagonist) led to reduced tumor volumes and lower serum CCL2 compared to controls. The dual regimen of carlumab plus XCT790 produced the most substantial reductions in both metrics. Similarly, in endometrial cancer-derived organoids, co-treatment with XCT790 and carlumab exerted greater growth inhibition than individual agents. These observations indicate that ERRα blockade may impede progression by disrupting mitochondrial OXPHOS, thereby diminishing CCL2 production. Prior reports have noted that ERRα suppression enhances chemosensitivity in endometrial cancer [28] and improves outcomes when combined with endocrine therapy over endocrine treatment alone [48]. Recent evidence from PD-1-resistant melanoma models shows ERRα inhibition aids therapy by impairing tumor energetics while promoting immune activation—via cytokine induction for macrophage repolarization and enhanced antigen presentation to boost CD8+ T cell recruitment [14]. These align with our data, highlighting ERRα as a potential key target for metabolic modulation and immune microenvironment remodeling in future endometrial cancer strategies.

Lipid profiling further showed elevated cardiolipin (CL) and phosphatidylglycerol (PG) in cells overexpressing ERRα or PTPMT1. Notably, upregulated CL species in these conditions were enriched for saturated fatty acids. As essential components of the mitochondrial inner membrane [49], CLs with higher saturation exhibit reduced fluidity [50], potentially accounting for the observed increases in cristae density and OXPHOS efficiency upon ERRα or PTPMT1 elevation. This offers novel insights into how ERRα-PTPMT1 orchestration of CL dynamics and mitochondrial integrity influences metabolic support for tumor advancement, suggesting additional avenues for targeted interventions in endometrial cancer.

Study limitations include the single-center origin of patient data from Fujian Maternal and Child Health Hospital, with a constrained cohort size that could introduce selection bias. Established markers like CA125, Ki67, estrogen receptor (ER), and progesterone receptor (PR) have recognized prognostic limitations in routine practice. Molecular pathway details remain incompletely defined. Our CCL2-focused analysis centered on tumor cells, without evaluating CCR2 or related receptors on macrophages or their functional states. Clinical experience with carlumab indicates limited efficacy and potential CCL2 rebound upon discontinuation, necessitating further optimization before combining with XCT790.

Conclusion

In conclusion, integrating proteomics, lipidomics, and cytokine profiling, we reveal ERRα's PTPMT1-dependent role in bridging endometrial cancer metabolism and immunity. We delineate how ERRα-PTPMT1 enhances CL production to stabilize mitochondrial inner membranes, driving OXPHOS, ROS generation, NF-κB activation, and CCL2 upregulation. These insights lay groundwork for innovative therapies merging metabolic targeting and immunotherapy, offering hope for improved management of endometrial cancer patients.

Acknowledgments: None

Conflict of Interest: None

Financial Support: This study was funded by the National Key Research and Development Program of China (grant number: 2022YFC2704303); the National Natural Science Foundation of China (grant number: 82203739); the Startup Fund for Scientific Research, Fujian Medical University (grant number: 2022QH2045); Joint Funds for the Innovation of Science and Technology, Fujian Province (grant number: 2020Y9160, 2021Y9157, 2024Y9585).

Ethics Statement: This retrospective study was approved by the Ethics Committee of Fujian Maternal and Child Health Hospital (No. 2023KY117). Participants gave informed consent to participate in the study before taking part.

References

1. Crosbie EJ, Kitson SJ, McAlpine JN, et al. Endometrial cancer. Lancet. 2022;399:1412–28. doi: 10.1016/S0140-6736(22)00323-3
2. Lu KH, Broaddus RR. Endometrial Cancer. N Engl J Med. 2020;383:2053–64. doi: 10.1056/NEJMra1514010
3. Gao M, Sun P, Wang J, et al. Expression of estrogen receptor-related receptor isoforms and clinical significance in endometrial adenocarcinoma. Int J Gynecol Cancer. 2006;16:827–33. doi: 10.1111/j.1525-1438.2006.00527.x
4. Mao X, Lei H, Yi T, et al. Lipid reprogramming induced by the TFEB-ERRα axis enhanced membrane fluidity to promote EC progression. J Exp Clin Cancer Res. 2022;41:28. doi: 10.1186/s13046-021-02211-2
5. Li M, Yu Y, Xue K, et al. Genistein mitigates senescence of bone marrow mesenchymal stem cells via ERRα-mediated mitochondrial biogenesis and mitophagy in ovariectomized rats. Redox Biol. 2023;61:102649. doi: 10.1016/j.redox.2023.102649
6. Ren M, Phoon CKL, Schlame M. Metabolism and function of mitochondrial cardiolipin. Prog Lipid Res. 2014;55:1–16. doi: 10.1016/j.plipres.2014.04.001
7. Yu W-M, Liu X, Shen J, et al. Metabolic regulation by the mitochondrial phosphatase PTPMT1 is required for hematopoietic stem cell differentiation. Cell Stem Cell. 2013;12:62–74. doi: 10.1016/j.stem.2012.11.022
8. Du J-X, Luo Y-H, Zhang S-J, et al. Splicing factor SRSF1 promotes breast cancer progression via oncogenic splice switching of PTPMT1. J Exp Clin Cancer Res. 2021;40:171. doi: 10.1186/s13046-021-01978-8
9. Wang Y, Lei J, Zhang S, et al. 4EBP1 senses extracellular glucose deprivation and initiates cell death signaling in lung cancer. Cell Death Dis. 2022;13:1075. doi: 10.1038/s41419-022-05466-5
10. Bao MH-R, Yang C, Tse AP-W, et al. Genome-wide CRISPR-Cas9 knockout library screening identified PTPMT1 in cardiolipin synthesis is crucial to survival in hypoxia in liver cancer. Cell Rep. 2021;34:108676. doi: 10.1016/j.celrep.2020.108676
11. Huang X-D, Xiao F-J, Guo Y-T, et al. Protein tyrosine phosphatase 1 protects human pancreatic cancer from erastin-induced ferroptosis. Asian J Surg. 2022;45:2214–23. doi: 10.1016/j.asjsur.2021.11.048
12. Griveau A, Devailly G, Eberst L, et al. The PLA2R1-JAK2 pathway upregulates ERRα and its mitochondrial program to exert tumor-suppressive action. Oncogene. 2016;35:5033–42. doi: 10.1038/onc.2016.43
13. Feng Z, Zhang X, Zhou J, et al. An in vitro-transcribed circular RNA targets the mitochondrial inner membrane cardiolipin to ablate EIF4G2+/PTBP1+ pan-adenocarcinoma. Nat Cancer . 2024;5:30–46. doi: 10.1038/s43018-023-00650-8
14. Sahu A, Wang X, Munson P, et al. Discovery of Targets for Immune-Metabolic Antitumor Drugs Identifies Estrogen-Related Receptor Alpha. Cancer Discov. 2023;13:672–701. doi: 10.1158/2159-8290.CD-22-0244
15. Ren X, Liang J, Zhang Y, et al. Single-cell transcriptomic analysis highlights origin and pathological process of human endometrioid endometrial carcinoma. Nat Commun. 2022;13:6300. doi: 10.1038/s41467-022-33982-7
16. Ren F, Wang L, Wang Y, et al. Single-cell transcriptome profiles the heterogeneity of tumor cells and microenvironments for different pathological endometrial cancer and identifies specific sensitive drugs. Cell Death Dis. 2024;15:571. doi: 10.1038/s41419-024-06960-8

17. Mirza MR, Chase DM, Slomovitz BM, et al. Dostarlimab for Primary Advanced or Recurrent Endometrial Cancer. N Engl J Med. 2023;388:2145–58. doi: 10.1056/NEJMoa2216334
18. Cassetta L, Pollard JW. A timeline of tumour-associated macrophage biology. Nat Rev Cancer. 2023;23:238–57. doi: 10.1038/s41568-022-00547-1
19. Espinosa I, José Carnicer M, Catasus L, et al. Myometrial invasion and lymph node metastasis in endometrioid carcinomas: tumor-associated macrophages, microvessel density, and HIF1A have a crucial role. Am J Surg Pathol. 2010;34:1708–14. doi: 10.1097/PAS.0b013e3181f32168
20. Kübler K, Ayub TH, Weber SK, et al. Prognostic significance of tumor-associated macrophages in endometrial adenocarcinoma. Gynecol Oncol. 2014;135:176–83. doi: 10.1016/j.ygyno.2014.08.028
21. Yuk J-M, Kim TS, Kim SY, et al. Orphan Nuclear Receptor ERRα Controls Macrophage Metabolic Signaling and A20 Expression to Negatively Regulate TLR-Induced Inflammation. Immunity. 2015;43:80–91. doi: 10.1016/j.immuni.2015.07.003
22. The Cancer Genome Atlas Research Network Erratum: Integrated genomic characterization of endometrial carcinoma. Nature New Biol. 2013;500:242. doi: 10.1038/nature12325
23. Murray PJ. Macrophage Polarization. Annu Rev Physiol. 2017;79:541–66. doi: 10.1146/annurev-physiol-022516-034339
24. Gentek R, Molawi K, Sieweke MH. Tissue macrophage identity and self-renewal. Immunol Rev. 2014;262:56–73. doi: 10.1111/imr.12224.
25. Kameoka S, Adachi Y, Okamoto K, et al. Phosphatidic Acid and Cardiolipin Coordinate Mitochondrial Dynamics. Trends Cell Biol. 2018;28:67–76. doi: 10.1016/j.tcb.2017.08.011
26. Chen Z, Zhu S, Wang H, et al. PTPMT1 Is Required for Embryonic Cardiac Cardiolipin Biosynthesis to Regulate Mitochondrial Morphogenesis and Heart Development. Circulation. 2021;144:403–6. doi: 10.1161/CIRCULATIONAHA.121.054768
27. Asehnoune K, Strassheim D, Mitra S, et al. Involvement of reactive oxygen species in Toll-like receptor 4-dependent activation of NF-kappa B. J Immunol. 2004;172:2522–9. doi: 10.4049/jimmunol.172.4.2522
28. Su P, Mao X, Ma J, et al. ERRα promotes glycolytic metabolism and targets the NLRP3/caspase-1/GSDMD pathway to regulate pyroptosis in endometrial cancer. J Exp Clin Cancer Res. 2023;42:274. doi: 10.1186/s13046-023-02834-7
29. Hanahan D, Weinberg RA. Hallmarks of cancer: the next generation. Cell. 2011;144:646–74. doi: 10.1016/j.cell.2011.02.013
30. Biswas SK. Metabolic Reprogramming of Immune Cells in Cancer Progression. Immunity. 2015;43:435–49. doi: 10.1016/j.immuni.2015.09.001
31. Kuntz EM, Baquero P, Michie AM, et al. Targeting mitochondrial oxidative phosphorylation eradicates therapy-resistant chronic myeloid leukemia stem cells. Nat Med. 2017;23:1234–40. doi: 10.1038/nm.4399
32. Kim SH, Li M, Trousil S, et al. Phenformin Inhibits Myeloid-Derived Suppressor Cells and Enhances the Anti-Tumor Activity of PD-1 Blockade in Melanoma. J Invest Dermatol. 2017;137:1740–8. doi: 10.1016/j.jid.2017.03.033
33. Victorino VJ, Barroso WA, Assunção AKM, et al. PGC-1β regulates HER2-overexpressing breast cancer cells proliferation by metabolic and redox pathways. Tumour Biol. 2016;37:6035–44. doi: 10.1007/s13277-015-4449-0
34. Houtkooper RH, Vaz FM. Cardiolipin, the heart of mitochondrial metabolism. Cell Mol Life Sci. 2008;65:2493–506. doi: 10.1007/s00018-008-8030-5
35. Wei C, Yang C, Wang S, et al. Crosstalk between cancer cells and tumor associated macrophages is required for mesenchymal circulating tumor cell-mediated colorectal cancer metastasis. Mol Cancer. 2019;18:64. doi: 10.1186/s12943-019-0976-4
36. Kitamura T, Qian B-Z, Soong D, et al. CCL2-induced chemokine cascade promotes breast cancer metastasis by enhancing retention of metastasis-associated macrophages. J Exp Med. 2015;212:1043–59. doi: 10.1084/jem.20141836
37. Wang L, Zheng W, Zhang S, et al. Expression of monocyte chemotactic protein-1 in human endometrial cancer cells and the effect of treatment with tamoxifen or buserelin. J Int Med Res. 2006;34:284–90. doi: 10.1177/147323000603400307
38. Peña CG, Nakada Y, Saatcioglu HD, et al. LKB1 loss promotes endometrial cancer progression via CCL2-dependent macrophage recruitment. J Clin Invest. 2015;125:4063–76. doi: 10.1172/JCI82152

39. Obr AE, Kumar S, Chang Y-J, et al. Insulin-like growth factor receptor signaling in breast tumor epithelium protects cells from endoplasmic reticulum stress and regulates the tumor microenvironment. Breast Cancer Res. 2018;20:138. doi: 10.1186/s13058-018-1063-2
40. Méndez-Samperio P, Pérez A, Alba L. Reactive oxygen species-activated p38/ERK 1/2 MAPK signaling pathway in the Mycobacterium bovis bacillus Calmette Guérin (BCG)-induced CCL2 secretion in human monocytic cell line THP-1. Arch Med Res. 2010;41:579–85. doi: 10.1016/j.arcmed.2010.10.009
41. Singh S, Anshita D, Ravichandiran V. MCP-1: Function, regulation, and involvement in disease. Int Immunopharmacol. 2021;101:107598. doi: 10.1016/j.intimp.2021.107598
42. Ueno T, Toi M, Saji H, et al. Significance of macrophage chemoattractant protein-1 in macrophage recruitment, angiogenesis, and survival in human breast cancer. Clin Cancer Res. 2000;6:3282–9
43. Qian B-Z, Li J, Zhang H, et al. CCL2 recruits inflammatory monocytes to facilitate breast-tumour metastasis. Nature New Biol. 2011;475:222–5. doi: 10.1038/nature10138
44. Bonapace L, Coissieux M-M, Wyckoff J, et al. Cessation of CCL2 inhibition accelerates breast cancer metastasis by promoting angiogenesis. Nature New Biol. 2014;515:130–3. doi: 10.1038/nature13862
45. Loberg RD, Ying C, Craig M, et al. CCL2 as an Important Mediator of Prostate Cancer Growth In Vivo through the Regulation of Macrophage Infiltration. Neoplasia. 2007;9:556–62. doi: 10.1593/neo.07307
46. Li X, Yao W, Yuan Y, et al. Targeting of tumour-infiltrating macrophages via CCL2/CCR2 signalling as a therapeutic strategy against hepatocellular carcinoma. Gut. 2017;66:157–67. doi: 10.1136/gutjnl-2015-310514
47. Zhao L, Lim SY, Gordon-Weeks AN, et al. Recruitment of a myeloid cell subset (CD11b/Gr1 mid) via CCL2/CCR2 promotes the development of colorectal cancer liver metastasis. Hepatology. 2013;57:829–39. doi: 10.1002/hep.26094
48. Mao X, Dong B, Gao M, et al. Dual targeting of estrogen receptor α and estrogen-related receptor α: a novel endocrine therapy for endometrial cancer. Onco Targets Ther. 2019;12:6757–67. doi: 10.2147/OTT.S216146
49. Falabella M, Vernon HJ, Hanna MG, et al. Cardiolipin, Mitochondria, and Neurological Disease. Trends in Endocrinology & Metabolism. 2021;32:224–37. doi: 10.1016/j.tem.2021.01.006
50. Arellano H, Nardello-Rataj V, Szunerits S, et al. Saturated long chain fatty acids as possible natural alternative antibacterial agents: Opportunities and challenges. Adv Colloid Interface Sci. 2023;318:102952. doi: 10.1016/j.cis.2023.102952